nanomaterials

MDPI

Article

Device Simulation of Highly Stable and 29% Efficient $FA_{0.75}MA_{0.25}Sn_{0.95}Ge_{0.05}I_3$-Based Perovskite Solar Cell

Hussein Sabbah * and Zaher Abdel Baki

College of Engineering and Technology, American University of the Middle East, Egaila 54200, Kuwait; zaher.abdelbaki@aum.edu.kw

* Correspondence: hussein.sabbah@aum.edu.kw

Abstract: A new type of perovskite solar cell based on mixed tin and germanium has the potential to achieve good power conversion efficiency and extreme air stability. However, improving its efficiency is crucial for practical application in solar cells. This paper presents a quantitative analysis of lead-free $FA_{0.75}MA_{0.25}Sn_{0.95}Ge_{0.05}I_3$ using a solar cell capacitance simulator to optimize its structure. Various electron transport layer materials were thoroughly investigated to enhance efficiency. The study considered the impact of energy level alignment between the absorber and electron transport layer interface, thickness and doping concentration of the electron transport layer, thickness and defect density of the absorber, and the rear metal work function. The optimized structures included poly (3,4-ethylenedioxythiophene)polystyrene sulfonate (PEDOT:PSS) as the hole transport layer and either zinc oxide (ZnO) or zinc magnesium oxide ($Zn_{0.7}Mg_{0.3}O$) as the electron transport layer. The power conversion efficiency obtained was 29%, which was over three times higher than the initial structure. Performing numerical simulations on $FA_{0.75}MA_{0.25}Sn_{0.95}Ge_{0.05}I_3$ can significantly enhance the likelihood of its commercialization. The optimized values resulting from the conducted parametric study are as follows: a short-circuit current density of 30.13 $mA{\cdot}cm^{-2}$), an open-circuit voltage of 1.08 V, a fill factor of 86.56%, and a power conversion efficiency of 28.31% for the intended solar cell.

Keywords: solar cell; photovoltaics; thin films; SCAPS simulation; lead-free perovskite; power conversion efficiency; Sn:Ge perovskite

Citation: Sabbah, H.; Baki, Z.A. Device Simulation of Highly Stable and 29% Efficient $FA_{0.75}MA_{0.25}Sn_{0.95}Ge_{0.05}I_3$-Based Perovskite Solar Cell. *Nanomaterials* **2023**, *13*, 1537. https://doi.org/10.3390/nano13091537

Academic Editors: Salvo Mirabella and Giacometta Mineo

Received: 10 April 2023
Revised: 27 April 2023
Accepted: 29 April 2023
Published: 3 May 2023

1. Introduction

Renewable energy has become a crucial aspect of global energy production due to the increasing demand for clean and sustainable sources of energy. Research into solar cell technology is highly appealing and holds great promise, since sunlight is an unlimited and free resource that is both fundamentally renewable and environmentally friendly in contrast to finite fossil fuels [1,2]. In this context, the use of metal halide perovskites (MHP) in photovoltaics has seen tremendous growth in the past 10 years, with the recent power conversion efficiency (PCE) reaching above 25% [3–5]. Despite this progress, the challenge lies in the fact that all the current MHP used to achieve high PCE contain lead, making it doubtful that this technology will be adopted on a large scale, especially in Europe, where strict regulations against the use of lead in electronics have been put in place [6].

As a result, there has been a growing interest in recent years to replace the lead component (Pb) in the perovskite formula $APbX_3$ with less toxic elements such as tin (Sn), bismuth (Bi), antimony (Sb), copper (Cu), or germanium (Ge) for both photovoltaic applications and crystal formation [7]. Of these alternatives, Sn-based perovskites [8,9] have been the most extensively studied and have demonstrated impressive PCE of up to 13% [10]. Sn-based perovskites have the advantage of smaller optical bandgaps [11–13] and greater charge mobility [14] compared to their Pb-based counterparts, making them ideal for single junction solar cells and all-perovskite tandem solar cells. Additionally, Sn is

a naturally abundant element that does not present any environmental or health hazards. Perovskite solar cells (PSCs) based on Sn are widely recognized for their instability when exposed to the air due to the tendency of Sn to oxidize from a +2 to +4 state, which results in the creation of oxygen vacancies that can act as traps [2,15,16].

Another potential replacement for lead is Ge, a group 14 elements such as Sn and Pb. Germanium is a strong candidate for perovskite solar cells, as it has a higher electronegativity and more covalent character than lead [13]. Despite numerous theoretical studies suggesting the potential of germanium halide perovskites for solar cell applications [17–20], they have only rarely been studied experimentally due to their mercurial character in a +2 oxidation state [21]. To date, the PCE of Ge-based PSC is still below 5% due to factors such as a smaller ionic radius, limited solubility in polar solvents, and a relatively wide bandgap (>1.6 eV) [18,22,23]. Although lead-free perovskites have demonstrated good efficiencies, there remains a persistent need to improve their stability and effectiveness [24–27], as their power conversion efficiency (PCE) values still fall considerably below the Shockley–Queisser efficiency limit of 33.7% [28] for a single junction. It is important to note that this limit has been exceeded by using nanoscale metallization in perovskite solar cells [28–31]. However, although metallization represents progress in perovskite technology, it is unlikely to significantly change the market situation for these cells. The primary challenge for perovskite cells is their poor durability and rapid degradation in the presence of oxygen and atmospheric water. To address the issue of oxidation in PSC, various techniques have been explored [16,32–35], including changing the electronic structure of the perovskite material, the encapsulation of PSC, incorporating hydrogen bonding, and applying a hydrophobic layer, among others [32,36].

One of the techniques for enhancing the performance of PSC involves mixing cations in tin–germanium Sn:Ge-based PSC. This has shown positive results in the literature [17,37–39]. By changing the Sn:Ge ratio, researchers have been able to achieve a lower bandgap and improved stability [40]. According to a study by Ito et al. [38], the efficiency of pure Sn-based perovskites improved from 3.31% to 4.48% (and even further to 6.90% after 72 h) when 5% germanium was doped into the material. The measurement was taken in the air without encapsulation. The addition of germanium is believed to have increased the stability of the perovskite structure while decreasing the trap density. This trend was also observed by Ng et al. [39], as they recorded the highest PCE (7.9%) of Sn:Ge-based PSC to date. The efficiency of the Sn:Ge-based PSC is significantly lower than that of the Pb-based version due to low V_{oc} and J_{sc}. This is likely caused by poor absorption at the UV range, as noted in prior research [41–43], and issues with the energy level alignment at the interface electron transport layer (ETL)/perovskite [44,45].

Further improvement in the PCE is still required, as the experimental outcomes have yet to reach the 25% PCE recorded by lead-based perovskite solar cells [44]. Studying the properties of the materials used in solar cells and controlling them through reliable simulation software can result in the creation of solar cells that are both highly efficient and cost-effective. PSC simulation is an interesting and straightforward process that can be carried out using various trustworthy programs such as SCAPS, AFORS-HET, Sentarus, and Silvaco [43,46–49].

In this contribution, we aim to enhance the efficiency of $FA_{0.75}MA_{0.25}Sn_{0.95}Ge_{0.05}I_3$-based solar cells by utilizing SCAPS software, developed by Gent University [50]. This particular perovskite has demonstrated a good PCE of 7.9% and impressive air stability in previous experiments [38,39]. This study presents a simple yet comprehensive simulation of the $FA_{0.75}MA_{0.25}Sn_{0.95}Ge_{0.05}I_3$-based PSC with a conventional (n-i-p) planar structure, which has not been previously conducted. The simulation mainly focuses on the use of metal oxide transport layers, particularly ZnO and $Zn_{0.7}Mg_{0.3}O$. These materials have suitable electronic energies, high transparency, and uniform substrate coverage, making them excellent candidates for an ETL in the low-cost and large-scale production of lead-free PSC [51,52].

To attain maximum efficiency, an optimization process is carried out. First, a range of ETL materials are evaluated, and the most suitable ones are chosen. Then, their thicknesses and doping concentrations are optimized. Following this, the thickness of the perovskite absorber layer and its defect density are optimized. The effect of the rear metal work function on the photovoltaic performance of the device is analyzed subsequently. Finally, the results of the optimized structure are presented, demonstrating an improvement in efficiency of around 29%.

2. Materials and Methods

The design and performance analysis of a solar cell were conducted using the SCAPS-1D software program. This numerical simulation tool was developed by researchers in the Department of Electronics and Information Systems (ELIS) at the University of Gent in Belgium [50]. The simulation program solves Poisson's equation and the continuity equation for free electrons and holes in the conduction and valence bands. It enables the computation and observation of various electrical properties and parameters, such as the current density–voltage characteristics (J–V curve), the energy band structure of the heterojunction, quantum efficiency (QE), open circuit voltage (V_{oc}), short circuit current (Jsc), current density, power conversion efficiency (PCE), and fill factor (FF), among others. All simulations were conducted at a temperature of 300 K under the standard illumination of 1000 W/m^2 and an air mass of AM 1.5 G. The absorber layer was sandwiched between the hole transport layer (HTL) and ETL layers.

Figure 1 illustrates the proposed PSC structure with fluorine − dopedtinoxide(FTO)/ETL/$FA_{0.75}MA_{0.25}Sn_{0.95}Ge_{0.05}I_3$/(PEDOT : PSS)/Gold(Au). The solar cell has a conventional structure (n-i-p), meaning that light enters the cell from the ETL side, with FTO acting as the front contact and Au as the back contact. For the HTL, PEDOT : PSS is used in every structure. However, instead of using organic ETLs fullerene (C60) and [6,6]-phenyl-C(61)-butyric acid methyl ester (PCBM), as in the experimental work, this study investigated two ideal ETLs, ZnO and $Zn_{0.7}Mg_{0.3}O$, as well as the conventional and extensively studied ETL titanium dioxide (TiO_2). The photovoltaic performance of the cell was compared using three different metal oxides (TiO_2, ZnO, and $Zn_{0.7}Mg_{0.3}O$), alternately used as the ETL layer with the two organic ETLs C60 and PCBM.

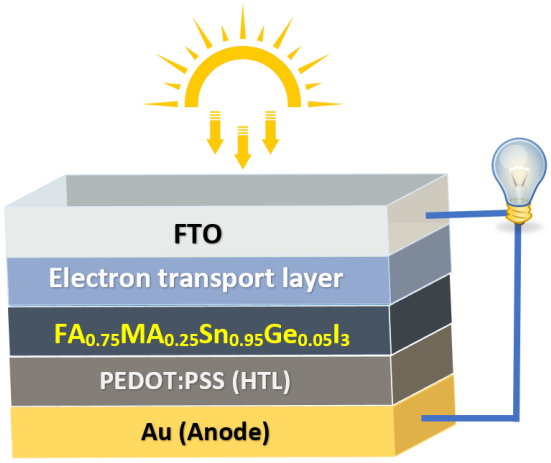

Figure 1. Schematic diagram of a PSC based on mixed Sn:Ge $FA_{0.75}MA_{0.25}Sn_{0.95}Ge_{0.05}I_3$.

The energy level diagram of the perovskite with two organic ETLs and three inorganic metal oxide ETLs, along with other layers, is depicted in Figure 2.

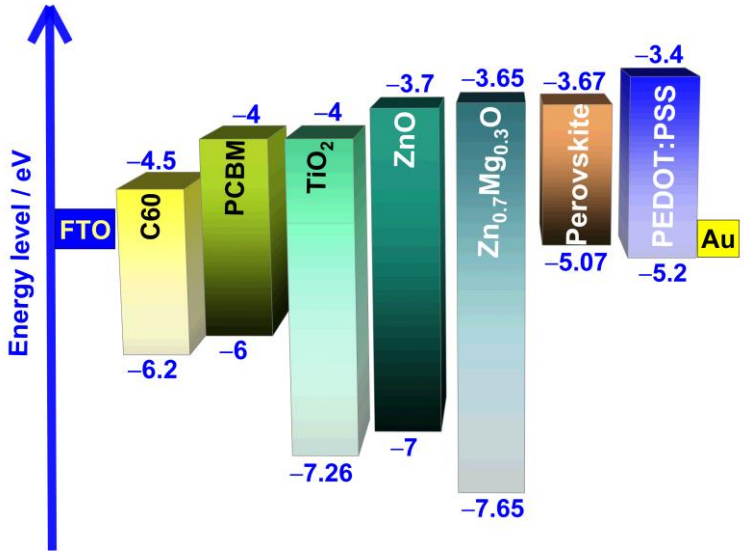

Figure 2. Band alignment between the ETL materials and $FA_{0.75}MA_{0.25}Sn_{0.95}Ge_{0.05}I_3$ perovskite.

Tables 1–3 provide a summary of the device and material parameters that were taken from theories, experiments, and the literature. The parameters listed in the table were considered while creating the initial setup for the simulation process. Various properties, such as the thickness and doping concentration of the ETL, the thickness and defect density of the absorber layer, and the rear metal work function, were adjusted to achieve the best possible outcome and to examine their impact on the device's performance.

Table 1. Electrical and optical properties employed in the simulation of $FA_{0.75}MA_{0.25}Sn_{0.95}Ge_{0.05}I_3$-based PSC.

Parameters	C60 (ETL) [53–56]	$FA_{0.75}MA_{0.25}Sn_{0.95}Ge_{0.05}I_3$ (Aborsober) [38,39,57]	PEDOT : PSS (HTL) [53–56]
Thickness (μm)	0.05	0.4	0.05
Bandgap E_g(eV)	1.7	1.4	1.8
Electron Affinity χ (eV)	4.50	3.670	3.40
Dielectric permittivity	18	8.2	18
CB effective density of states (cm^{-3})	2.2×10^{18}	2.2×10^{18}	2.2×10^{18}
VB effective density of states (cm^{-3})	1.8×10^{19}	1.8×10^{19}	1.8×10^{19}
Electron mobility $(cm^2/V.s)$	8×10^{-2}	2	4.5×10^{-2}
Hole mobility $(cm^2/V.s)$	8×10^{-2}	2	4.5×10^{-2}
Donor Concentration N_D (cm^{-3})	1×10^{17}	1×10^{13}	1×10^{7}
Acceptor concentration N_A (cm^{-3})	0	0	1×10^{18}

Aside from the earlier study that involved altering the ETL materials, various parameters, including the thickness and doping concentration of the ideal ETL layers and absorber, the defect density of the perovskite layer, and the rear metal work function of the cells, were adjusted to evaluate their effects on the device's performance. The goal was to achieve the most effective cell structure through these modifications.

Table 2. Electrical and optical properties of different ETL materials.

Parameters	PCBM [53–56]	TiO_2 [42,58]	ZnO [59,60]	$Zn_{0.7}Mg_{0.3}O$ [56,61,62]
Thickness (μm)	0.05	0.05	0.05	0.05
Bandgap E_g (eV)	2	3.26	3.3	4
Electron Affinity χ (eV)	4	4	3.7	3.65
Dielectric permittivity	3.9	32	9	8
CB effective density of states (cm^{-3})	2.5×10^{21}	2.2×10^{18}	2.2×10^{18}	2.2×10^{18}
VB effective density of states (cm^{-3})	2.5×10^{21}	1.8×10^{19}	1.8×10^{19}	1.8×10^{19}
Electron mobility $(cm^2/V.s)$	2.5×10^{-2}	20	100	100
Hole mobility $(cm^2/V.s)$	2.5×10^{-2}	10	25	25
Donor Concentration N_D (cm^{-3})	1×10^{17}	1×10^{17}	1×10^{17}	1×10^{17}
Acceptor concentration N_A (cm^{-3})	0	0	0	0

Table 3. Defect density values inside the layers and at the interface of the cell.

Parameters	ETL	HTL	Perovskite	HTL/Perovskite	Perovskite/ETL
Defect Type	Neutral	Neutral	Neutral	Neutral	Neutral
Capture cross-section for electrons σ_n (cm^{-2})	1×10^{-15}	1×10^{-15}	1×10^{-15}	1×10^{-18}	1×10^{-15}
Capture cross-section for hole σ_p (cm^{-2})	1×10^{-15}	1×10^{-15}	1×10^{-15}	1×10^{-16}	1×10^{-15}
Energetic distribution	Single	Single	Gaussian	Single	Single
Energy level with respect to E_v (above E_v) (eV)	0.6	0.650	0.6	0.6	0.6
Characteristic energy (eV)	0.1	0.1	0.1	0.1	0.1
Total density N_t (cm^{-3})	1×10^{15}	1×10^{15}	1×10^{16}	1×10^{12}	1×10^{12}

3. Results and Discussion

In this section, the study's findings are presented, which started by examining the impact of different ETLs on the solar cell performance. After identifying the best structures based on this analysis, the research then explored various factors. These included optimizing the thickness and doping concentration of the ideal ETL, refining the absorber thickness, assessing the effect of the absorber layer's defect density, and investigating how the solar cell's performance was affected by the rear metal work function.

3.1. Impact of ETL Material on Solar Cell Performance

In planar PSC, the interface between the ETL and perovskite absorber layer plays a vital role in determining their overall performance [45]. To ensure high-quality ETL, several properties must be considered [44]. Firstly, the ETL should possess a suitable lowest unoccupied molecular orbital (LUMO) energy level that matches the conduction band energy of perovskite materials. Secondly, it should have high electron mobility and photochemical stability under solar irradiation. Lastly, it should be optically transparent to ensure maximum light absorption by the perovskite layer in the n-i-p PSC. Therefore, various ETLs, including, C60, PCBM, TiO_2, ZnO, and $Zn_{0.7}Mg_{0.3}O$, are being examined to investigate how device performances differ with the uses of different ETLs. The electrical and optical parameters of the ETLs are listed in Table 2. Figure 3 depicts both the impact of the ETL material on the current density–voltage characteristics and its effect on the PCE.

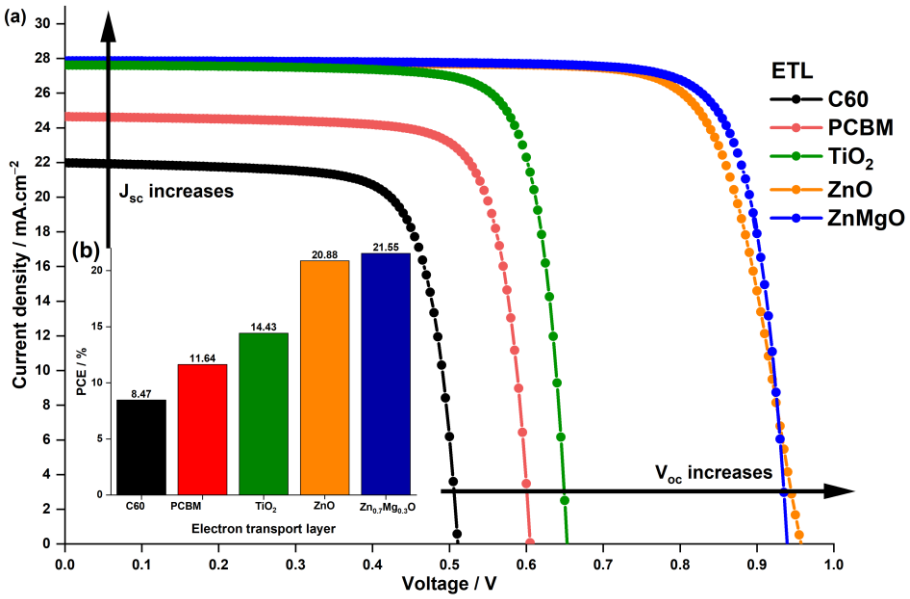

Figure 3. Impact of the ETL material on (**a**) the current density–voltage characteristics and (**b**) the PCE of the PSC.

Table 4 lists the solar cell performance metrics, as well as the conduction band offset (CBO) values, for the simulated devices with five different ETLs. CBO refers to the difference in electron affinity between the absorber and the ETL (Equation (1)).

$$\text{CBO} = \chi_{absorber} - \chi_{ETL} \quad (1)$$

Figure 3 clearly shows that PSC with the organic ETL materials C60 and PCBM have low performance, yielding PCE values below 12%. In contrast, all the structures with inorganic ETL materials produce PCE values above 14%. Among the structures simulated, those incorporating ZnO ETL and $Zn_{0.7}Mg_{0.3}O$ ETL materials are the most efficient, achieving PCE values of 20.88% and 21.55%, respectively.

Table 4. Conduction band offset for the ETL materials and their photovoltaic properties.

ETL	CBO/eV	*PCE*/%	V_{oc}/V	J_{sc}/mA·cm^{-3}	*FF*/%
C60	−0.83	8.47	0.51	21.97	75.43
PCBM	−0.33	11.64	0.60	24.64	78.09
TiO_2	−0.33	14.43	0.65	27.61	80.02
ZnO	−0.02	20.88	0.95	27.75	78.61
$Zn_{0.7}Mg_{0.3}O$	0.02	21.55	0.94	27.86	82.33

Devices incorporating organic ETLs and TiO_2 ETL exhibit significantly lower PCEs than PSCs utilizing ZnO ETL and ZnMgO ETL, primarily due to their lower V_{oc}. The low V_{oc} is likely attributable to the band alignment present within their structure. Table 4 reveals that, as the CBO becomes increasingly negative, the V_{oc} value decreases correspondingly. PSCs incorporating ZnO ETL or $Zn_{0.7}Mg_{0.3}O$ ETL, on the other hand, exhibit CBO values close to zero or even positive, which accounts for their comparatively higher V_{oc} values. When the conduction band minimum (CBM) of the ETL is located below that of the absorber, it results in a negative CBO, and a cliff-like structure forms at the heterojunction ETL/absorber. In solar cells, this cliff structure is detrimental, since it promotes the accumulation of electrons and holes near the interface following charge separation, leading to greater charge recombination via the interface's deep-level defects, which results in lower V_{oc}.

Alongside the band alignment within the structure of the PSC, another factor that could contribute to the difference in behavior between the devices is the ETL's bandgap. A suitable ETL material must possess optical transparency to ensure maximum light absorption by the perovskite layer in the n-i-p PSC, which leads to the generation of more electrons and ultimately results in a higher J_{sc} achieved by the cell. This claim is supported by Figure 3 and Table 4. PSCs with organic ETLs, which have bandgap values of 1.7 eV and 2 eV, respectively, demonstrate the lowest values of J_{sc}, specifically 21.97 mA·cm^{-2} and 24.64 mA·cm^{-2}. Conversely, PSCs with inorganic metal oxide ETLs score the highest values of J_{sc}, above 27 mA·cm^{-2}, as they have bandgap values above 2.8 eV.

Figure 4 endorses this observation, illustrating the quantum efficiency of PSCs with various ETLs. PSCs with organic ETLs have a notably low quantum efficiency, particularly for wavelengths below 700 nm, attributable to their below −2 eV bandgap values. On the other hand, PSCs with inorganic metal oxide ETLs exhibit the highest quantum efficiency, since their bandgap values exceed 2.8 eV.

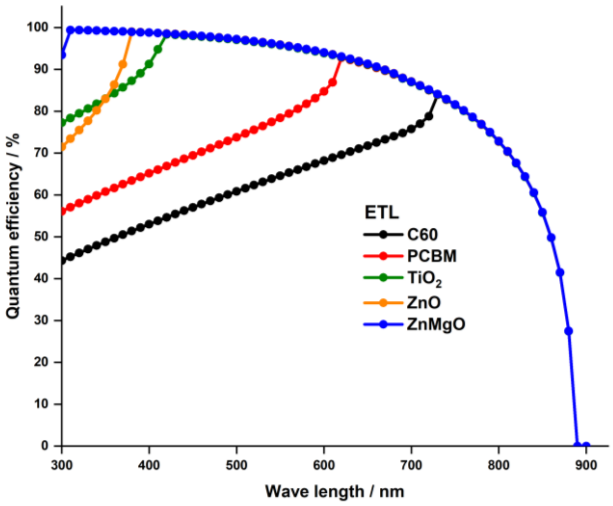

Figure 4. Quantum efficiency for the simulated devices with different ETL materials.

The results presented in this section demonstrate that ZnO and $Zn_{0.7}Mg_{0.3}O$ outperform the other tested ETLs. Consequently, the study investigates how the thickness and doping concentration of these ETL materials affect the performances of solar cell devices.

3.1.1. Impact of ETL Thickness

In the previous analysis, we compared the ETL materials while keeping the layer thickness constant at 50 nm. However, in this section, we study the impact of varying the thickness of the ETL on the solar cell's performance. We varied the ETL thickness from 50 nm to 200 nm and analyzed the photovoltaic performances. Figure 5 shows the results as a function of the ETL thickness. The V_{oc} and PCE of both devices remain constant and independent of an ETL thickness up to around 160 nm. However, they decrease significantly as the thickness increases further. The increase in thickness causes electrons to travel a longer distance to reach the top electrode, resulting in a higher likelihood of electron recombination with minority carriers (holes). This, in turn, causes the V_{oc} to decline sharply. Additionally, the cell with a ZnO ETL shows a noticeable decrease in J_{sc}, likely due to a decrease in light transmittance through the ZnO layer.

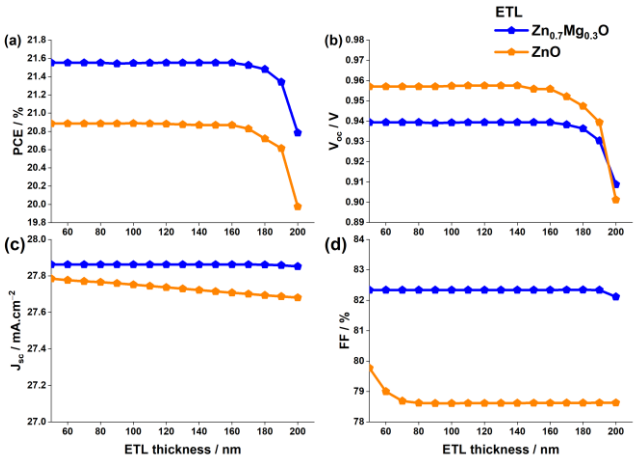

Figure 5. Variations of (**a**) PCE, (**b**) V_{oc}, (**c**) J_{sc}, and (**d**) FF as a function of the ETL thickness for the two ETL materials ZnO and $Zn_{0.7}Mg_{0.3}O$.

This decrease in light transmittance is confirmed by Figure 6, which shows the quantum efficiency of the cells as a function of the ETL thickness. The QE and the J_{sc} of the cell with a Zn_0.7Mg_0.3O ETL remain unchanged due to the wide bandgap of $Zn_{0.7}Mg_{0.3}O$ (4.1 eV).

It is clear that the photovoltaic parameters deteriorate as the ETL thickness increases, resulting in a decrease in PCE for both ETLs. This is caused by inefficient charge carrier transport to the electrodes, an increase in series resistance that reduces the fill factor FF, and a higher probability of recombination as the ETL thickness increases. Therefore, for the remainder of this study, a thickness of 50 nm is adopted. Any thinner layer may not fully cover the perovskite layer, causing direct contact between FTO and perovskite, which leads to carrier recombination and reduced hole-blocking efficiency [63].

3.1.2. Impact of ETL Doping Concentration

In addition to identifying the most suitable ETL materials, namely ZnO and $Zn_{0.7}Mg_{0.3}O$, and optimizing their thickness at 50 nm, it is important to consider the impact of the doping concentration N_D on the photovoltaic parameters of PSCs. In the previous sections, a fixed doping concentration of $N_D = 1 \times 10^{17}$ cm^{-3} was used for all materials tested. However, this section presents a study on the effect of varying the N_D from 1×10^{15} cm^{-3} to 1×10^{20} cm^{-3} for the current density–voltage characteristics and power conversion efficiency (PCE), as shown in Figure 7.

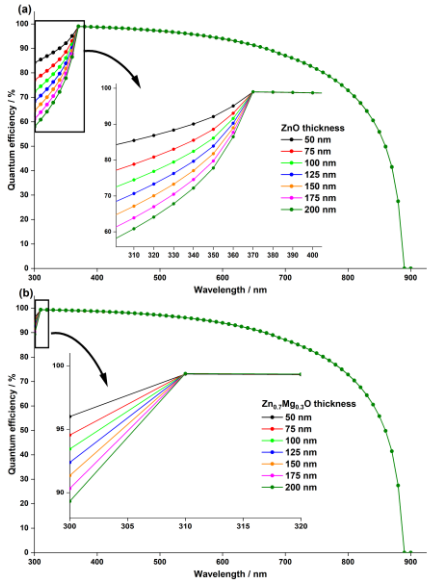

Figure 6. Effect of ETL thickness on the quantum efficiency of the PSC with two different ETL materials: (**a**) ZnO and (**b**) $Zn_{0.7}Mg_{0.3}O$.

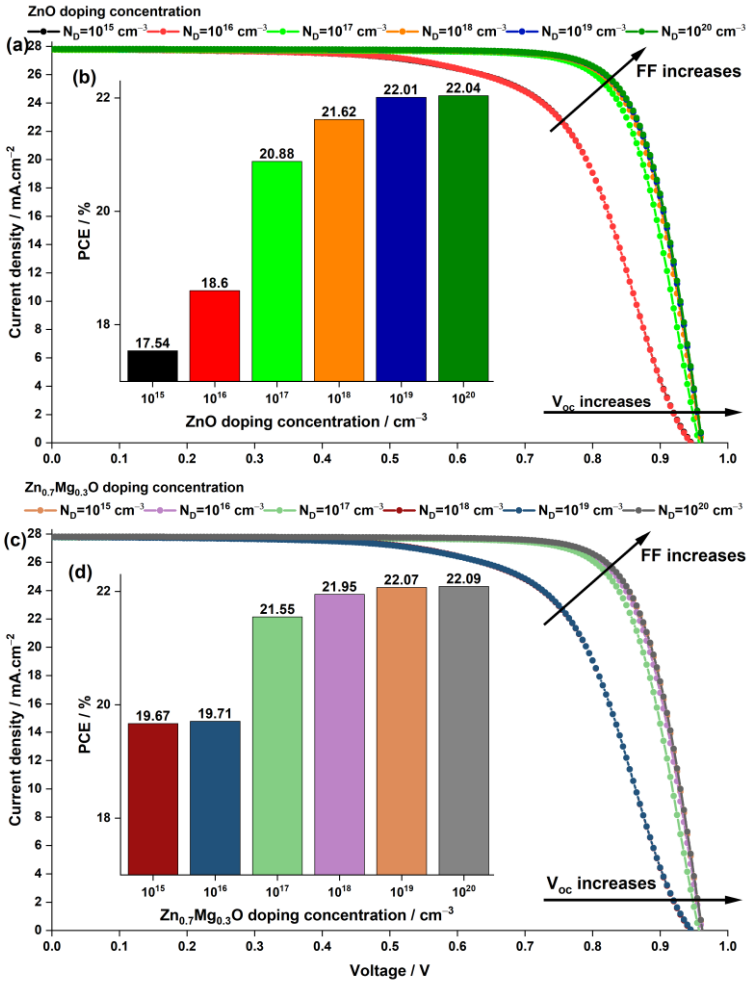

Figure 7. Effect of the doping concentration of the ETL ZnO on (**a**) the current density–voltage characteristics of the PSC and (**b**) the PCE, and the effect of the doping concentration of ETL$Zn_{0.7}Mg_{0.3}O$ on (**c**) the current density–voltage characteristics of the PSC and (**d**) the PCE.

The results shown in Figure 7 clearly demonstrate that increasing the doping concentration in the ETL significantly enhances the V_{oc} and FF of the cells, resulting in a higher PCE. Notably, the J_{sc} of both devices remains almost constant, as it has already reached a high value of approximately 28 mA·cm^{-2}, and the effect of doping on J_{sc} is negligible.

Both devices achieved a peak PCE of 22% at doping concentrations of 1×10^{19} cm^{-3} and 1×10^{20} cm^{-3}, with little difference between them. The improvement in V_{oc} and FF can be attributed to the effect of doping on the energy level alignment between the ETL and the perovskite layer, which enhances the charge transport properties and reduces the recombination losses.

Although increasing the doping concentration of the ETL improves the V_{oc}, FF, and overall efficiency of the PSC, the optimal doping concentration has been determined to be 1×10^{19} cm^{-3} due to practical manufacturing challenges. Higher doping concentrations are difficult to achieve practically and could potentially create deep Coulomb traps, which may adversely affect carrier mobility [64].

3.2. Effect of the Perovskite Layer on the Solar Cell Performance

In addition to the crucial role of ETL materials in improving the PSC performance, the absorber layer also has a significant impact on the efficiency of the solar cell. This section will examine how the absorber material $FA_{0.75}MA_{0.25}Sn_{0.95}Ge_{0.05}I_3$ affects the solar cell performance, with a specific focus on the thickness and defect density of this absorber.

3.2.1. Impact of Absorber Thickness

The thickness of the absorber layer in perovskite solar cells can significantly impact the device's performance, as it determines the amount of light absorption and the efficiency of the conversion process. It is crucial to maintain an optimal thickness range, because if the absorber layer is too thin, it may not absorb sufficient light to generate enough current. Conversely, if the absorber layer is too thick, the charge carriers generated by the absorbed light may struggle to travel through the material and reach the electrodes, leading to lower device efficiency. The previous analyses were performed using a 400 nm thick $FA_{0.75}MA_{0.25}Sn_{0.95}Ge_{0.05}I_3$. In this section, the impact of the absorber thickness on the solar cell's performance was studied by varying the thickness from 200 nm to 1500 nm. The results obtained for the photovoltaic outputs are shown in Figure 8, while Figure 9 displays the effect of the absorber thickness on the quantum efficiency with respect to the wavelengths of the light.

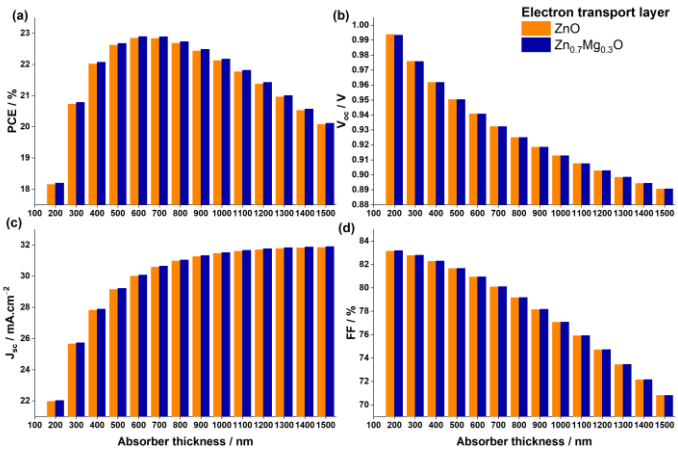

Figure 8. Impact of the absorber thickness on (**a**) PCE, (**b**) V_{oc}, (**c**) J_{sc}, and (**d**) FF for PSCs with the two ETL materials ZnO and $Zn_{0.7}Mg_{0.3}O$.

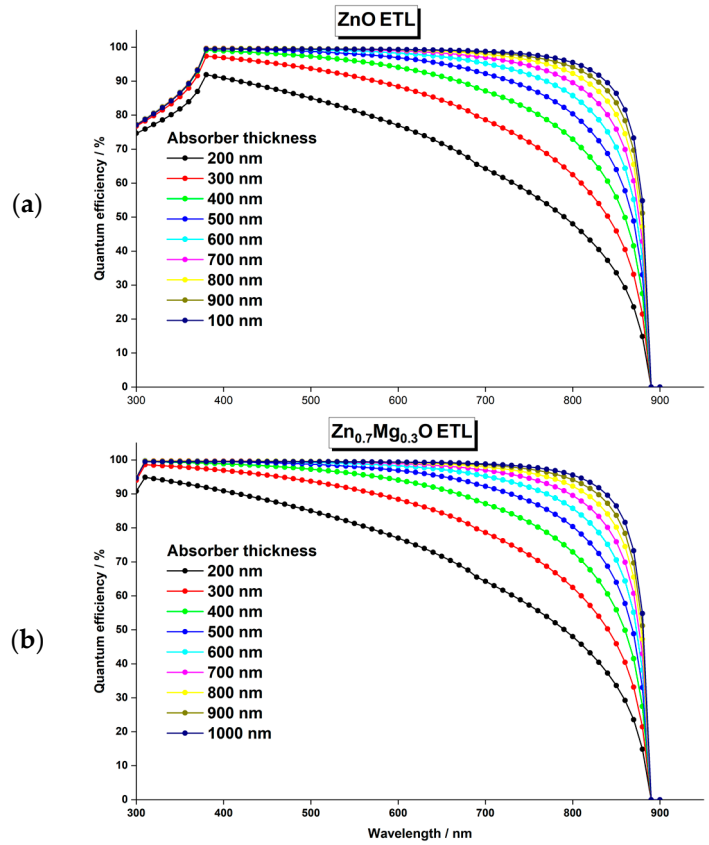

Figure 9. Impact of the absorber thickness on the quantum efficiency of PSCs with (**a**) ZnO ETL and (**b**) $Zn_{0.7}Mg_{0.3}O$ ETL.

By observing Figures 8 and 9, it is evident that the behavior of all photovoltaic parameters and the quantum efficiency as a function the of absorber thickness is similar for both devices, with ZnO ETL and $Zn_{0.7}Mg_{0.3}O$ ETL. The PCE of both devices steadily increases with the increasing thickness until it reaches a maximum value of 22.9% at 600 nm, beyond which it gradually decreases. This can be attributed to the opposing trends of the V_{oc} and the J_{sc}, which have the most significant impact on the PCE.

Firstly, a considerable increase in J_{sc} was observed in both devices by increasing the thickness of the absorber layer, but it reached saturation at 700 nm. Beyond this point, the effect of the absorber layer thickness became insignificant. This substantial enhancement of J_{sc} is attributed to the generation of additional electron–hole pairs in the perovskite, which occurred as a result of increased light absorption resulting from the thicker absorber layer. The increase in J_{sc} is supported by the higher QE of the device at larger thicknesses, as shown in Figure 9.

In contrast, the open-circuit voltage V_{oc} decreases as the absorber layer thickness increases. While a thicker layer allows for more photons to be absorbed and more electron–hole pairs to be generated, it also leads to a high density of defects that act as recombination centers. As a result, the lifetime of electron–hole pairs is reduced, and more pairs recombine before reaching the electrodes, causing a decline in the V_{oc}. In addition, the series resistance of the device increases with thicker absorber layers, further lowering the V_{oc} and the FF. Consequently, increasing the absorber layer thickness beyond 600 nm results in diminishing returns and decreases the overall efficiency of the solar cell.

3.2.2. Impact of Absorber Defect Density N_t

Although adjusting the thickness of the absorber has improved the efficiency of solar cells, further enhancements in the solar cell performance can be achieved by considering the defect density of the perovskite layer as an additional influential parameter.

The initial defect density N_t of the absorber was set at 1×10^{16} cm^{-3}, which is the same as the value obtained in the experiment conducted by Ng et al. [39] on $FA_{0.75}MA_{0.25}Sn_{0.95}Ge_{0.05}I_3$. Recent experimental studies by Zheng et al. [65] and Chen et al. [66] showed that the defect density in perovskite can be as low as 1×10^{11} cm^{-3} and 1×10^{12} cm^{-3}, respectively. In our simulation study, we varied the defect density between 1×10^{12} cm^{-3} and 1×10^{16} cm^{-3} and plotted the changes in the photovoltaic properties with N_t for devices using ZnO ETL and $Zn_{0.7}Mg_{0.3}O$ ETL in Figure 10.

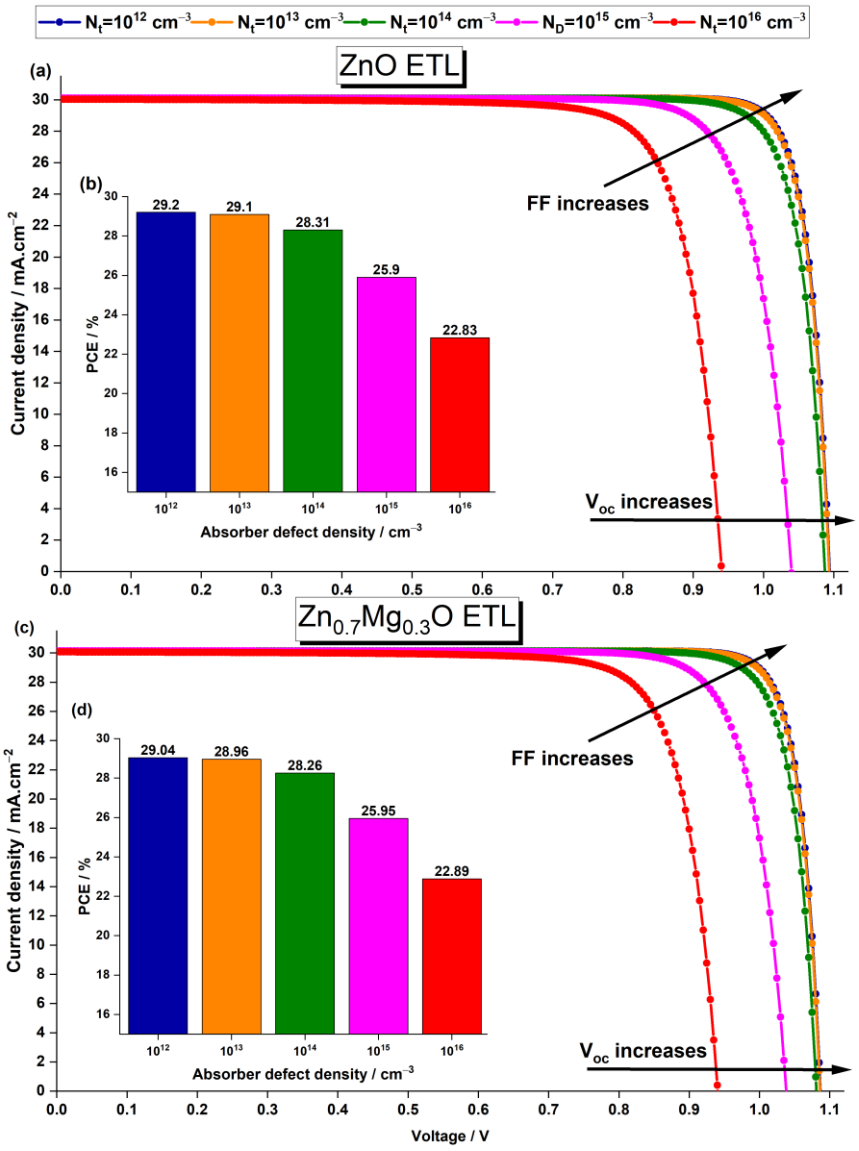

Figure 10. Effect of the absorber defect density on the current density–voltage characteristics and the PCE of the PSC with ZnO ETL (**a**,**b**) and $Zn_{0.7}Mg_{0.3}O$ ETL (**c**,**d**), respectively.

The J_{sc} of both devices remain constant, while V_{oc} and FF are greatly increased when the defect density in perovskite is reduced, resulting in a significant enhancement of the PCE. When the defect density reaches a low level of 1×10^{13} cm^{-3}, both cells show a significant improvement in performance. The cells with ZnO ETL and $Zn_{0.7}Mg_{0.3}O$ ETL exhibit a J_{sc} of 30.11 $mA.cm^{-2}$ and 30.11 $mA.cm^{-2}$, V_{oc} of 1.087 V and 1.087 V, FF of 86.46% and 86.74%, and PCE of 28.31% and 28.26%, respectively. However, further reducing the N_t from 1×10^{13} cm^{-3} to 1×10^{12} cm^{-3} only leads to a slight improvement in the cell performance. Hence, an absorber defect density $N_t = 1 \times 10^{13}$ cm^{-3} is adopted for the rest of this study.

The impact of perovskite defect density on the device performance can be explained by the Shockley–Read–Hall (SRH) recombination model [64,67]. To gain a better understanding of this effect, the relationship between the SRH recombination rate and depth from the surface for various defect densities was examined. Figure 11 illustrates these findings. The results indicate that recombination becomes more significant in the light-absorbing layer due to the higher defect density resulting from the low film quality. The defects in the absorber layer act as recombination centers for the electron–hole pairs generated by incident photons, which reduces the efficiency of the device. The defect density in the absorber layer can be influenced by a variety of factors, such as the synthesis process, the perovskite composition, and the deposition method. Therefore, greater efforts should be made to improve the fabrication technique of solar cells.

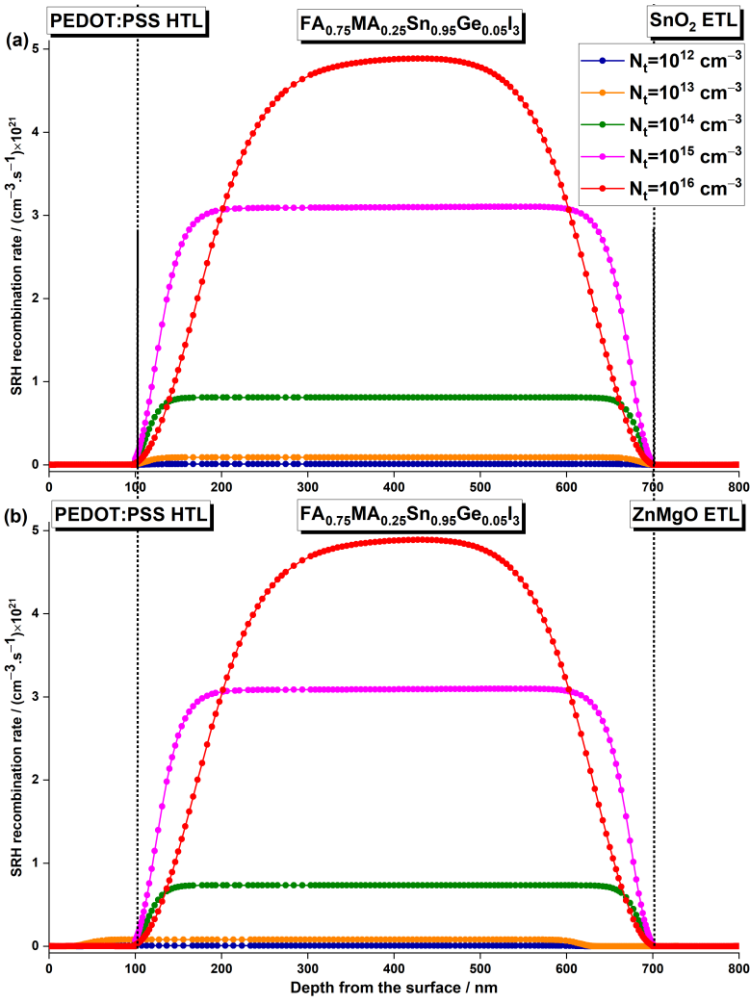

Figure 11. Effect of the absorber layer defect density on the recombination rate with the depth from the surface of the PSC with (**a**) ZnO ETL and (**b**) $Zn_{0.7}Mg_{0.3}O$ ETL.

3.3. Impact of Rear Electrode Work Function

The work function of the rear metal in a PSC plays a critical role in determining the energy alignment at the interface between the HTL and the rear contact electrode, which affects the built-in potential V_{bi} and the charge carrier extraction. In this study, the rear electrode in the PSC was initially made of gold (Au), which is a common choice for metal back contact. However, other materials such as aluminum (Al), silver (Ag), chromium (Cr), nickel (Ni), palladium (Pd), and platinum (Pt), with different work functions ranging from 4.2 to 5.7 eV, are also used in PSCs and optoelectronic devices. Table 5 presents the work functions of several chosen metals in the field [68].

Table 5. Conduction band offset for the ETL materials and their photovoltaic properties.

Metal	Al	Ag	Cr	Au	Ni	Pd	Pt
work function $\varnothing_M$/eV	4.125	4.26	4.4	5.1	5.15	5.3	5.15

Our study aimed to examine how the rear metal work function affects the photovoltaic properties of the devices. The results are depicted in Figure 12.

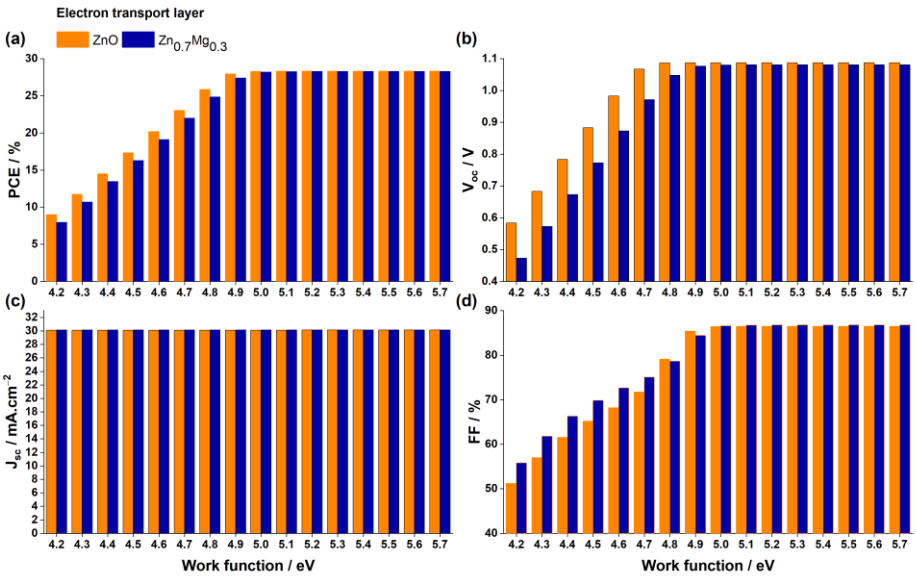

Figure 12. Impact of the work function of the anode on the (**a**) PCE, (**b**) V_{oc}, (**c**) J_{sc}, and (**d**) FF for PSCs with the two ETL materials ZnO and $Zn_{0.7}Mg_{0.3}O$.

As the work function of the anode increases, both the V_{oc} and FF of the solar cell increase, resulting in greater efficiency, until they reach a maximum and plateau at 5 eV and above. This is because a decrease in the metal work function reduces the built-in electric field in the absorber layer, causing a poor collection of photo-generated carriers and resulting in lower V_{oc} and FF.

In cases where the anode's work function is lower than that of PEDOT:PSS (5.0 eV) (5.0 eV) [69], with metals such as Ag, Cu, and Au, a rectifying Schottky barrier contact is created at the anode–PEDOT interface. This contact acts as an obstacle to the movement of holes to the anode, thereby decreasing the V_{oc}, FF, and PCE, as illustrated in Figure 12. On the other hand, when using an anode made of Au, Ni, Pd, or Pt, which have a higher work function than PEDOT, an ohmic contact is established at the anode–PEDOT:PSS interface. This enables efficient hole transport across the interface, resulting in higher V_{oc}, FF, and PCE values in the PSC. Therefore, selecting one of these anodes is crucial when manufacturing the solar cell device.

4. Conclusions

Despite conducting extensive experimental studies on $FA_{0.75}MA_{0.25}Sn_{0.95}Ge_{0.05}I_3$-based PSCs, the highest achieved PCE remained below 8%, which falls short of the desired benchmark for commercial applications. Our work utilized SCAPS-1D software to simulate a conventional (n-i-p) structure and systematically compared the effectiveness of various ETL materials. Specifically, we tested two organic ETLs and three inorganic metal oxide ETLs while keeping the other layers unchanged. Our findings showed that selecting appropriate ETL materials could significantly increase the PCE of the cell to 21%. The ZnO and $Zn_{0.7}Mg_{0.3}O$ ETLs were found to be the most effective ETL materials due to their excellent band alignments with the absorber and wide bandgaps. The efficiency of the

solar cell was further improved by increasing the doping concentration of the ETL and the absorber thickness, reducing the absorber defect density, and selecting gold or any metal with a work function greater than 5.1 eV. These enhancements led to an unprecedented PCE of almost 29%. It is crucial to be cautious while interpreting these findings, because they may not accurately represent the experimental efforts, which were only able to achieve a maximum PCE of less than 8%. Future research should focus on refining the device fabrication techniques, as our novel results could provide a feasible approach to develop cost-effective, highly efficient, and stable $FA_{0.75}MA_{0.25}Sn_{0.95}Ge_{0.05}I_3$-based PSCs.

Author Contributions: Conceptualization, H.S.; methodology, H.S.; software, H.S.; validation, H.S.; formal analysis, H.S.; investigation, H.S.; resources, H.S.; data curation, H.S.; writing—original draft preparation, H.S.; writing—review and editing, H.S. and Z.A.B.; visualization, H.S. and Z.A.B.; supervision, H.S.; and project administration, H.S. All authors have read and agreed to the published version of the manuscript.

Funding: This research received no external funding.

Institutional Review Board Statement: Not applicable.

Informed Consent Statement: Not applicable.

Data Availability Statement: Not applicable.

Acknowledgments: The author would like to acknowledge Marc Burgelman (University of Gent) for providing the simulation software SCAPS.

Conflicts of Interest: The authors declare no conflict of interest.

References

1. Yang, Z.; Guo, Y.; Li, H.; Zhou, Y.; Zuo, X.; Yu, Y.; Pan, C.; Strzalka, J.; Nam, C.-Y.; Rafailovich, M.H. Roles of Interfacial Tension in Regulating Internal Organization of Low Bandgap Polymer Bulk Heterojunction Solar Cells by Polymer Additives. *Adv. Mater. Interfaces* **2018**, *5*, 1800435. [CrossRef]
2. Noel, N.K.; Stranks, S.D.; Abate, A.; Wehrenfennig, C.; Guarnera, S.; Haghighirad, A.-A.; Sadhanala, A.; Eperon, G.E.; Pathak, S.K.; Johnston, M.B.; et al. Lead-Free Organic–Inorganic Tin Halide Perovskites for Photovoltaic Applications. *Energy Environ. Sci.* **2014**, *7*, 3061–3068. [CrossRef]
3. Kim, J.Y.; Lee, J.-W.; Jung, H.S.; Shin, H.; Park, N.-G. High-Efficiency Perovskite Solar Cells. *Chem. Rev.* **2020**, *120*, 7867–7918. [CrossRef] [PubMed]
4. Liang, F.-C.; Jhuang, F.-C.; Fang, Y.-H.; Benas, J.-S.; Chen, W.-C.; Yan, Z.-L.; Lin, W.-C.; Su, C.-J.; Sato, Y.; Chiba, T.; et al. Synergistic Effect of Cation Composition Engineering of Hybrid $Cs_{1-x}FA_xPbBr_3$ Nanocrystals for Self-Healing Electronics Application. *Adv. Mater.* **2023**, *35*, 2207617. [CrossRef] [PubMed]
5. Ma, C.; Park, N.-G. A Realistic Methodology for 30% Efficient Perovskite Solar Cells. *Chem* **2020**, *6*, 1254–1264. [CrossRef]
6. Abate, A. Perovskite Solar Cells Go Lead Free. *Joule* **2017**, *1*, 659–664. [CrossRef]
7. Mahajan, P.; Datt, R.; Chung Tsoi, W.; Gupta, V.; Tomar, A.; Arya, S. Recent Progress, Fabrication Challenges and Stability Issues of Lead-Free Tin-Based Perovskite Thin Films in the Field of Photovoltaics. *Coord. Chem. Rev.* **2021**, *429*, 213633. [CrossRef]
8. Sabbah, H.; Arayro, J.; Mezher, R. Numerical Simulation and Optimization of Highly Stable and Efficient Lead-Free Perovskite FA1−xCsxSnI3-Based Solar Cells Using SCAPS. *Materials* **2022**, *15*, 4761. [CrossRef]
9. Xu, K. Development of Tin-Based Perovskite Materials for Solar Cell Applications: A Minireview. *Instrum. Sci. Technol.* **2021**, *49*, 91–105. [CrossRef]
10. Cao, J.; Yan, F. Recent Progress in Tin-Based Perovskite Solar Cells. *Energy Environ. Sci.* **2021**, *14*, 1286–1325. [CrossRef]
11. Ke, W.; Kanatzidis, M.G. Prospects for Low-Toxicity Lead-Free Perovskite Solar Cells. *Nat. Commun.* **2019**, *10*, 965. [CrossRef]
12. Stoumpos, C.C.; Malliakas, C.D.; Kanatzidis, M.G. Semiconducting Tin and Lead Iodide Perovskites with Organic Cations: Phase Transitions, High Mobilities, and Near-Infrared Photoluminescent Properties. *Inorg. Chem.* **2013**, *52*, 9019–9038. [CrossRef] [PubMed]
13. Marshall, K.P.; Walker, M.; Walton, R.I.; Hatton, R.A. Enhanced Stability and Efficiency in Hole-Transport-Layer-Free CsSnI3 Perovskite Photovoltaics. *Nat. Energy* **2016**, *1*, 16178. [CrossRef]
14. Herz, L.M. Charge-Carrier Mobilities in Metal Halide Perovskites: Fundamental Mechanisms and Limits. *ACS Energy Lett.* **2017**, *2*, 1539–1548. [CrossRef]
15. Rajendra Kumar, G.; Kim, H.-J.; Karupannan, S.; Prabakar, K. Interplay between Iodide and Tin Vacancies in $CsSnI_3$ Perovskite Solar Cells. *J. Phys. Chem. C* **2017**, *121*, 16447–16453. [CrossRef]

16. Liao, Y.; Liu, H.; Zhou, W.; Yang, D.; Shang, Y.; Shi, Z.; Li, B.; Jiang, X.; Zhang, L.; Quan, L.N.; et al. Highly Oriented Low-Dimensional Tin Halide Perovskites with Enhanced Stability and Photovoltaic Performance. *J. Am. Chem. Soc.* **2017**, *139*, 6693–6699. [CrossRef]
17. Ju, M.-G.; Dai, J.; Ma, L.; Zeng, X.C. Lead-Free Mixed Tin and Germanium Perovskites for Photovoltaic Application. *J. Am. Chem. Soc.* **2017**, *139*, 8038–8043. [CrossRef]
18. Stoumpos, C.C.; Frazer, L.; Clark, D.J.; Kim, Y.S.; Rhim, S.H.; Freeman, A.J.; Ketterson, J.B.; Jang, J.I.; Kanatzidis, M.G. Hybrid Germanium Iodide Perovskite Semiconductors: Active Lone Pairs, Structural Distortions, Direct and Indirect Energy Gaps, and Strong Nonlinear Optical Properties. *J. Am. Chem. Soc.* **2015**, *137*, 6804–6819. [CrossRef] [PubMed]
19. Ming, W.; Shi, H.; Du, M.-H. Large Dielectric Constant, High Acceptor Density, and Deep Electron Traps in Perovskite Solar Cell Material CsGeI3. *J. Mater. Chem. A* **2016**, *4*, 13852–13858. [CrossRef]
20. Sun, P.-P.; Li, Q.-S.; Yang, L.-N.; Li, Z.-S. Theoretical Insights into a Potential Lead-Free Hybrid Perovskite: Substituting Pb^{2+} with Ge^{2+}. *Nanoscale* **2016**, *8*, 1503–1512. [CrossRef]
21. Ansari, M.I.H.; Qurashi, A.; Nazeeruddin, M.K. Frontiers, Opportunities, and Challenges in Perovskite Solar Cells: A Critical Review. *J. Photochem. Photobiol. C Photochem. Rev.* **2018**, *35*, 1–24. [CrossRef]
22. Gao, P.; Bin Mohd Yusoff, A.R.; Nazeeruddin, M.K. Dimensionality Engineering of Hybrid Halide Perovskite Light Absorbers. *Nat. Commun.* **2018**, *9*, 5028. [CrossRef]
23. Krishnamoorthy, T.; Ding, H.; Yan, C.; Leong, W.L.; Baikie, T.; Zhang, Z.; Sherburne, M.; Li, S.; Asta, M.; Mathews, N.; et al. Lead-Free Germanium Iodide Perovskite Materials for Photovoltaic Applications. *J. Mater. Chem. A* **2015**, *3*, 23829–23832. [CrossRef]
24. Mei, A.; Li, X.; Liu, L.; Ku, Z.; Liu, T.; Rong, Y.; Xu, M.; Hu, M.; Chen, J.; Yang, Y.; et al. A Hole-Conductor–Free, Fully Printable Mesoscopic Perovskite Solar Cell with High Stability. *Science* **2014**, *345*, 295–298. [CrossRef]
25. Arya, S.; Mahajan, P.; Gupta, R.; Srivastava, R.; Tailor, N.K.; Satapathi, S.; Sumathi, R.R.; Datt, R.; Gupta, V. A Comprehensive Review on Synthesis and Applications of Single Crystal Perovskite Halides. *Prog. Solid State Chem.* **2020**, *60*, 100286. [CrossRef]
26. Grätzel, M. The Light and Shade of Perovskite Solar Cells. *Nat. Mater* **2014**, *13*, 838–842. [CrossRef] [PubMed]
27. Boix, P.P.; Agarwala, S.; Koh, T.M.; Mathews, N.; Mhaisalkar, S.G. Perovskite Solar Cells: Beyond Methylammonium Lead Iodide. *J. Phys. Chem. Lett.* **2015**, *6*, 898–907. [CrossRef]
28. Jacak, J.E.; Jacak, W.A. Routes for Metallization of Perovskite Solar Cells. *Materials* **2022**, *15*, 2254. [CrossRef] [PubMed]
29. Wu, R.; Yang, B.; Zhang, C.; Huang, Y.; Cui, Y.; Liu, P.; Zhou, C.; Hao, Y.; Gao, Y.; Yang, J. Prominent Efficiency Enhancement in Perovskite Solar Cells Employing Silica-Coated Gold Nanorods. *J. Phys. Chem. C* **2016**, *120*, 6996–7004. [CrossRef]
30. Laska, M.; Krzemińska, Z.; Kluczyk-Korch, K.; Schaadt, D.; Popko, E.; Jacak, W.A.; Jacak, J.E. Metallization of Solar Cells, Exciton Channel of Plasmon Photovoltaic Effect in Perovskite Cells. *Nano Energy* **2020**, *75*, 104751. [CrossRef]
31. Yao, K.; Zhong, H.; Liu, Z.; Xiong, M.; Leng, S.; Zhang, J.; Xu, Y.; Wang, W.; Zhou, L.; Huang, H.; et al. Plasmonic Metal Nanoparticles with Core–Bishell Structure for High-Performance Organic and Perovskite Solar Cells. *ACS Nano* **2019**, *13*, 5397–5409. [CrossRef]
32. Shao, S.; Liu, J.; Portale, G.; Fang, H.-H.; Blake, G.R.; ten Brink, G.H.; Koster, L.J.A.; Loi, M.A. Highly Reproducible Sn-Based Hybrid Perovskite Solar Cells with 9% Efficiency. *Adv. Energy Mater.* **2018**, *8*, 1702019. [CrossRef]
33. Lee, S.J.; Shin, S.S.; Kim, Y.C.; Kim, D.; Ahn, T.K.; Noh, J.H.; Seo, J.; Seok, S.I. Fabrication of Efficient Formamidinium Tin Iodide Perovskite Solar Cells through SnF2–Pyrazine Complex. *J. Am. Chem. Soc.* **2016**, *138*, 3974–3977. [CrossRef] [PubMed]
34. Chen, K.; Wu, P.; Yang, W.; Su, R.; Luo, D.; Yang, X.; Tu, Y.; Zhu, R.; Gong, Q. Low-Dimensional Perovskite Interlayer for Highly Efficient Lead-Free Formamidinium Tin Iodide Perovskite Solar Cells. *Nano Energy* **2018**, *49*, 411–418. [CrossRef]
35. Ke, W.; Stoumpos, C.C.; Zhu, M.; Mao, L.; Spanopoulos, I.; Liu, J.; Kontsevoi, O.Y.; Chen, M.; Sarma, D.; Zhang, Y.; et al. Enhanced Photovoltaic Performance and Stability with a New Type of Hollow 3D Perovskite {en}$FASnI_3$. *Sci. Adv.* **2017**, *3*, e1701293. [CrossRef] [PubMed]
36. Wang, F.; Ma, J.; Xie, F.; Li, L.; Chen, J.; Fan, J.; Zhao, N. Organic Cation-Dependent Degradation Mechanism of Organotin Halide Perovskites. *Adv. Funct. Mater.* **2016**, *26*, 3417–3423. [CrossRef]
37. Sabbah, H. Numerical Simulation of 30% Efficient Lead-Free Perovskite $CsSnGeI_3$-Based Solar Cells. *Materials* **2022**, *15*, 3229. [CrossRef]
38. Ito, N.; Kamarudin, M.A.; Hirotani, D.; Zhang, Y.; Shen, Q.; Ogomi, Y.; Iikubo, S.; Minemoto, T.; Yoshino, K.; Hayase, S. Mixed Sn–Ge Perovskite for Enhanced Perovskite Solar Cell Performance in Air. *J. Phys. Chem. Lett.* **2018**, *9*, 1682–1688. [CrossRef]
39. Ng, C.H.; Nishimura, K.; Ito, N.; Hamada, K.; Hirotani, D.; Wang, Z.; Yang, F.; Likubo, S.; Shen, Q.; Yoshino, K.; et al. Role of GeI2 and SnF2 Additives for SnGe Perovskite Solar Cells. *Nano Energy* **2019**, *58*, 130–137. [CrossRef]
40. Chen, M.; Ju, M.-G.; Garces, H.F.; Carl, A.D.; Ono, L.K.; Hawash, Z.; Zhang, Y.; Shen, T.; Qi, Y.; Grimm, R.L.; et al. Highly Stable and Efficient All-Inorganic Lead-Free Perovskite Solar Cells with Native-Oxide Passivation. *Nat. Commun.* **2019**, *10*, 16. [CrossRef]
41. Baig, F.; Khattak, Y.H.; Marí, B.; Beg, S.; Ahmed, A.; Khan, K. Efficiency Enhancement of $CH_3NH_3SnI_3$ Solar Cells by Device Modeling. *J. Electron. Mater.* **2018**, *47*, 5275–5282. [CrossRef]
42. Du, H.-J.; Wang, W.-C.; Zhu, J.-Z. Device Simulation of Lead-Free $CH_3NH_3SnI_3$ Perovskite Solar Cells with High Efficiency. *Chin. Phys. B* **2016**, *25*, 108802. [CrossRef]
43. Sabbah, H.; Arayro, J.; Mezher, R. Simulation and Investigation of 26% Efficient and Robust Inverted Planar Perovskite Solar Cells Based on $GA_{0.2}FA_{0.78}SnI_3$-1%EDAI2 Films. *Nanomaterials* **2022**, *12*, 3885. [CrossRef]

44. Pan, H.; Zhao, X.; Gong, X.; Li, H.; Ladi, N.H.; Zhang, X.L.; Huang, W.; Ahmad, S.; Ding, L.; Shen, Y.; et al. Advances in Design Engineering and Merits of Electron Transporting Layers in Perovskite Solar Cells. *Mater. Horiz.* **2020**, *7*, 2276–2291. [CrossRef]
45. Ding, C.; Zhang, Y.; Liu, F.; Kitabatake, Y.; Hayase, S.; Toyoda, T.; Yoshino, K.; Minemoto, T.; Katayama, K.; Shen, Q. Effect of the Conduction Band Offset on Interfacial Recombination Behavior of the Planar Perovskite Solar Cells. *Nano Energy* **2018**, *53*, 17–26. [CrossRef]
46. Minemoto, T.; Kawano, Y.; Nishimura, T.; Chantana, J. Numerical Reproduction of a Perovskite Solar Cell by Device Simulation Considering Band Gap Grading. *Opt. Mater.* **2019**, *92*, 60–66. [CrossRef]
47. Gagandeep; Singh, M.; Kumar, R. Simulation of Perovskite Solar Cell with Graphene as Hole Transporting Material. *AIP Conf. Proc.* **2019**, *2115*, 030548. [CrossRef]
48. Nandal, V.; Nair, P.R. Predictive Modeling of Ion Migration Induced Degradation in Perovskite Solar Cells. *ACS Nano* **2017**, *11*, 11505–11512. [CrossRef] [PubMed]
49. Du, Y.; Cai, H.; Wen, H.; Wu, Y.; Li, Z.; Xu, J.; Huang, L.; Ni, J.; Li, J.; Zhang, J. Revealing the Unfavorable Role of Superfluous $CH_3NH_3PbI_3$ Grain Boundary Traps in Perovskite Solar Cells on Carrier Collection. *RSC Adv.* **2016**, *6*, 83264–83272. [CrossRef]
50. Burgelman, M.; Nollet, P.; Degrave, S. Modelling Polycrystalline Semiconductor Solar Cells. *Thin Solid Film.* **2000**, *361–362*, 527–532. [CrossRef]
51. Gamal, N.; Sedky, S.H.; Shaker, A.; Fedawy, M. Design of Lead-Free Perovskite Solar Cell Using $Zn_{1-x}Mg_xO$ as ETL: SCAPS Device Simulation. *Optik* **2021**, *242*, 167306. [CrossRef]
52. Rahman, M.S.; Miah, S.; Marma, M.S.W.; Sabrina, T. Simulation Based Investigation of Inverted Planar Perovskite Solar Cell with All Metal Oxide Inorganic Transport Layers. In Proceedings of the 2019 International Conference on Electrical, Computer and Communication Engineering (ECCE), Cox'sBazar, Bangladesh, 7–9 February 2019; pp. 1–6.
53. Dang, Y.; Zhou, Y.; Liu, X.; Ju, D.; Xia, S.; Xia, H.; Tao, X. Formation of Hybrid Perovskite Tin Iodide Single Crystals by Top-Seeded Solution Growth. *Angew. Chem. Int. Ed.* **2016**, *55*, 3447–3450. [CrossRef] [PubMed]
54. Jokar, E.; Chien, C.-H.; Tsai, C.-M.; Fathi, A.; Diau, E.W.-G. Robust Tin-Based Perovskite Solar Cells with Hybrid Organic Cations to Attain Efficiency Approaching 10%. *Adv. Mater.* **2019**, *31*, 1804835. [CrossRef]
55. Liu, X.; Yan, K.; Tan, D.; Liang, X.; Zhang, H.; Huang, W. Solvent Engineering Improves Efficiency of Lead-Free Tin-Based Hybrid Perovskite Solar Cells beyond 9%. *ACS Energy Lett.* **2018**, *3*, 2701–2707. [CrossRef]
56. Minemoto, T.; Kawano, Y.; Nishimura, T.; Shen, Q.; Yoshino, K.; Iikubo, S.; Hayase, S.; Chantana, J. Theoretical Analysis of Band Alignment at Back Junction in Sn–Ge Perovskite Solar Cells with Inverted p-i-n Structure. *Sol. Energy Mater. Sol. Cells* **2020**, *206*, 110268. [CrossRef]
57. Singh, N.; Agarwal, A.; Agarwal, M. Numerical Simulation of Highly Efficient Lead-Free All-Perovskite Tandem Solar Cell. *Sol. Energy* **2020**, *208*, 399–410. [CrossRef]
58. Stamate, M.D. On the Dielectric Properties of Dc Magnetron TiO_2 Thin Films. *Appl. Surf. Sci.* **2003**, *218*, 318–323. [CrossRef]
59. Doroody, C.; Rahman, K.S.; Rosly, H.N.; Harif, M.N.; Haque, F.; Tiong, S.K.; Amin, N. Impact of High Resistivity Transparent (HRT) Layer in Cadmium Telluride Solar Cells from Numerical Simulation. *J. Renew. Sustain. Energy* **2020**, *12*, 023702. [CrossRef]
60. Hoye, R.L.Z.; Ehrler, B.; Böhm, M.L.; Muñoz-Rojas, D.; Altamimi, R.M.; Alyamani, A.Y.; Vaynzof, Y.; Sadhanala, A.; Ercolano, G.; Greenham, N.C.; et al. Improved Open- Circuit Voltage in ZnO–PbSe Quantum Dot Solar Cells by Understanding and Reducing Losses Arising from the ZnO Conduction Band Tail. *Adv. Energy Mater.* **2014**, *4*, 1301544. [CrossRef] [PubMed]
61. Chantana, J.; Kato, T.; Sugimoto, H.; Minemoto, T. Structures of $Cu(In,Ga)(S,Se)_2$ Solar Cells for Minimizing Open-circuit Voltage Deficit: Investigation of Carrier Recombination Rates. *Prog. Photovolt. Res. Appl.* **2019**, *27*, 630–639. [CrossRef]
62. He, X.; Wu, L.; Hao, X.; Zhang, J.; Li, C.; Wang, W.; Feng, L.; Du, Z. The Band Structures of $Zn_{1-x}Mg_xO(In)$ and the Simulation of CdTe Solar Cells with a $Zn_{1-x}Mg_xO(In)$ Window Layer by SCAPS. *Energies* **2019**, *12*, 291. [CrossRef]
63. Onyeagba, C.R.; Islam, M.; Yarlagadda, P.K.D.V.; Tesfamichael, T. Investigating the Properties of Tin-Oxide Thin Film Developed by Sputtering Process for Perovskite Solar Cells. *Mater. Renew. Sustain. Energy* **2023**, *12*, 31–37. [CrossRef]
64. Abdelaziz, S.; Zekry, A.; Shaker, A.; Abouelatta, M. Investigating the Performance of Formamidinium Tin-Based Perovskite Solar Cell by SCAPS Device Simulation. *Opt. Mater.* **2020**, *101*, 109738. [CrossRef]
65. Zheng, X.; Chen, B.; Dai, J.; Fang, Y.; Bai, Y.; Lin, Y.; Wei, H.; Zeng, X.C.; Huang, J. Defect Passivation in Hybrid Perovskite Solar Cells Using Quaternary Ammonium Halide Anions and Cations. *Nat. Energy* **2017**, *2*, 17102. [CrossRef]
66. Chen, W.; Wu, Y.; Yue, Y.; Liu, J.; Zhang, W.; Yang, X.; Chen, H.; Bi, E.; Ashraful, I.; Grätzel, M.; et al. Efficient and Stable Large-Area Perovskite Solar Cells with Inorganic Charge Extraction Layers. *Science* **2015**, *350*, 944–948. [CrossRef] [PubMed]
67. Haider, S.Z.; Anwar, H.; Wang, M. A Comprehensive Device Modelling of Perovskite Solar Cell with Inorganic Copper Iodide as Hole Transport Material. *Semicond. Sci. Technol.* **2018**, *33*, 035001. [CrossRef]
68. Michaelson, H.B. The Work Function of the Elements and Its Periodicity. *J. Appl. Phys.* **1977**, *48*, 4729–4733. [CrossRef]
69. Mengistie, D.A.; Ibrahem, M.A.; Wang, P.-C.; Chu, C.-W. Highly Conductive PEDOT:PSS Treated with Formic Acid for ITO-Free Polymer Solar Cells. *ACS Appl. Mater. Interfaces* **2014**, *6*, 2292–2299. [CrossRef]